

Micro-defect imaging with an improved resolution using nonlinear ultrasonic Lamb waves

Cite as: J. Appl. Phys. **131**, 185101 (2022); doi: [10.1063/5.0087619](https://doi.org/10.1063/5.0087619)

Submitted: 7 February 2022 · Accepted: 24 April 2022 ·

Published Online: 9 May 2022



Weibin Li,¹ Jun Xiao,¹ and Mingxi Deng^{2,a)} 

AFFILIATIONS

¹School of Aerospace Engineering, Xiamen University, Xiamen 361005, China

²College of Aerospace Engineering, Chongqing University, Chongqing 400044, China

Note: This paper is part of the Special Topic on Non-Invasive and Non-Destructive Methods and Applications Part II.

a) Author to whom correspondence should be addressed: dengmx65@yahoo.com

ABSTRACT

Ultrasonic inspection is a widely used nondestructive testing approach in industrial fields for more accurate life prediction and efficient management strategies of critical structural components. However, it is quite challenging to detect a kind of micro-defect, whose size is much smaller than the ultrasonic wavelength but larger than the ultrasonic amplitude (namely, there is no appearance of non-classical acoustic nonlinearity). In this article, identification and imaging of a micro-defect of this size range with an improved resolution is conducted by the combination of the second-harmonic generation (SHG) of ultrasonic Lamb waves and the reconstruction algorithm for the probability inspection of damage. An intuitive model is first developed to explore the physical mechanism of a micro-defect-induced variation of generated second harmonic of a primary Lamb wave in a plate. Variations of amplitudes of second harmonics generated in propagation paths are used to construct the micro-defect image. A phase-reversal technique is employed to enhance the signal-to-noise ratio of the SHG. Comparisons between images constructed by linear and nonlinear acoustic features of Lamb wave propagation are presented. Results show that the image of the micro-defect with an improved resolution is successfully obtained by the proposed approach, while there is no visualized result obtained by the conventional linear ultrasonic one.

Published under an exclusive license by AIP Publishing. <https://doi.org/10.1063/5.0087619>

I. INTRODUCTION

Ultrasonic Lamb waves have been widely used in the field of nondestructive testing (NDT) as a solution to large component and structure inspection, which allows a large structure to be scanned without direct access.^{1,2} However, conventional linear ultrasonic Lamb wave techniques (such as wave velocity, linear resonance frequency, and attenuation measurements) are limited to realize macroscopic defect detection.³ It is known that the use of acoustic nonlinear response has a potential for micro-defect detection and material degradation characterization.^{4–7} Nonlinear ultrasonic Lamb wave techniques rely on the measurement of acoustic nonlinear response (such as second-harmonic waves) in relation to the micro-defect.^{8,9} It is well accepted that the sensitivity of nonlinear ultrasonic techniques to micro-defects is far higher than that of the linear ones.^{10–13}

The mechanism of non-classical acoustic nonlinearity for second-harmonic generation (SHG) has been well addressed to explain the interactions of defects with propagating ultrasonic

waves.¹⁴ However, the explanation is only available under the condition that the defect size is comparable with that of ultrasonic amplitude. If the defect size is much bigger than the wave amplitude but still much smaller than the ultrasonic wavelength, no measurable linear signal variation will be caused by the interactions of propagating waves with these kinds of micro-defects. Moreover, the well-accepted mechanism of non-classical acoustic nonlinearity for SHG induced by the micro-defect is not applicable for the defects of this size range. The micro-defect of this size range is of interest in this investigation. Micro-defects of this size range widely exist in industrial components, such as micro-notches, micro-corrosions, etc. Mechanisms for the use of SHG of Lamb waves to detect the micro-defects of this size range are still obscure. Moreover, it is quite challenging to detect these specific kinds of micro-defects.

The combination of the ultrasonic Lamb wave approach and the reconstruction algorithm for the probability inspection of damage (RAPID) has been successfully applied to the detection of

complex structures such as pipes and aircraft wings.^{15–19} The principle of this technique is based on the measure of the signal difference coefficient (SDC) on each propagation path for imaging.¹⁵ But, most of the earlier efforts focus on imaging of macro-defects using the variations of linear ultrasonic coefficients, such as wave amplitudes calculated in the time domain.^{16–19} Cross-interactions of micro-defects with propagating Lamb waves generally only result in the tiny variation in signals in the time domain, which could not be used for the reliable reconstruction of the micro-defect image with sufficient resolution. Recently, identification of micro-corrosions with regular and irregular shapes in metals has been successfully constructed by the combination of RAPID algorithm and SHG of the Rayleigh surface wave.²⁰ It has been proved that the SHG of ultrasonic waves can be taken as an effective means to identify the micro-defect.^{21–24} However, it is noticed that the second-harmonic amplitude is much smaller than that of the primary wave. Thus, it is easily overlooked that the effect of SHG is due to its tiny amplitude. It is necessary to enhance the amplitude of generated second harmonic. Phase-reversal technique or pulse-inversion technique has been successfully applied to double the even harmonics and offset the odd ones of ultrasonic waves.^{25,26}

It is known that in the process of SHG of Lamb wave propagation, the phase velocity difference between the primary Lamb wave and second harmonic generated in the propagation path will significantly affect the magnitude of generated second harmonic.²⁷ When the primary Lamb wave and second harmonic generated pass through the micro-defect, the phase velocity difference between them will be different from that where there is no micro-defect. This will induce the change in the amplitude of the generated second harmonic. Based on this consideration, combination of the effect of SHG of Lamb waves and the Lamb wave tomographic approach is employed to effectively identify and image the micro-defect in a metallic plate, where the width and depth of the micro-defect are smaller in one order of magnitude than the wavelength of both the primary Lamb wave and second harmonic. Lamb wave mode pair that approximately satisfies the phase velocity matching condition is intentionally selected to ensure the clear variation of the second harmonic generated in propagation paths with and without micro-defect. Variations of amplitudes of second harmonics generated are used to calculate the SDCs. Then, the SDC distribution on all paths of Lamb wave propagation is integrated to construct the image of the specimen with an artificial micro-defect. In addition, the phase-reversal approach is used to enhance the signal-to-noise ratio of the measured second harmonics. Image of the micro-defect is successfully obtained by the proposed approach with an improved resolution. Combination of the SHG of Lamb waves and the Lamb wave tomographic approach shows a potential for identification and imaging of the micro-defects, whose sizes are much smaller than the ultrasonic wavelength but larger than the ultrasonic amplitude.

II. THEORETICAL CONSIDERATIONS

A. SHG of Lamb wave

As shown in Fig. 1, the acoustic field of Lamb wave propagation in a plate can be taken as the sum of the primary wave \mathbf{u}_1 and

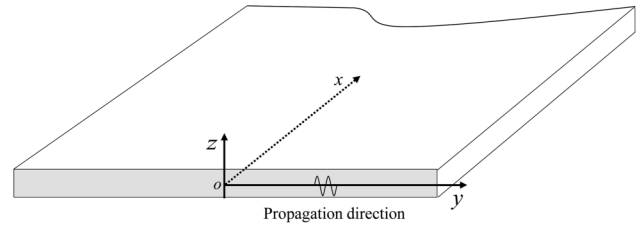


FIG. 1. Schematic of Lamb wave propagation in a plate.

the generated second harmonic \mathbf{u}_2 ,^{28–30}

$$\mathbf{u} = \mathbf{u}_1 + \mathbf{u}_2. \quad (1)$$

The primary Lamb wave at the fundamental frequency and second harmonic generated at the double frequency can be formally written as^{29,30}

$$\mathbf{u}_1 = \mathbf{u}(z)\exp[j(ky - \omega t)], \quad (2)$$

$$\mathbf{u}_2 = \sum_n A_n(y)\mathbf{u}_n^{(2)}(z)\exp(-2j\omega t), \quad (3)$$

where $\mathbf{u}(z)$ is the field function of the primary Lamb wave, $\mathbf{u}_n^{(2)}(z)$ is the field function of the n th second harmonic Lamb wave, and $A_n(y)$ is the corresponding expansion coefficient. Each secondary mode n enters the sum with its own modal expansion coefficient. The modal expansion coefficient of the n th mode can be expressed as^{29,30}

$$A_n(y) = \frac{(f_n^{\text{surf}} + f_n^{\text{vol}})}{4p_{nn}} \frac{\sin(\Delta_n y)}{\Delta_n} \exp[j(k_n^* + \Delta_n)y], \quad (4)$$

$$\Delta_n = (2k - k_n^*)/2, \quad (5)$$

where the terms f_n^{surf} and f_n^{vol} are defined as the complex external power due to surface traction and the volume force of second harmonic components generated by primary Lamb wave propagation in the y direction, respectively. k_n^* is the wavenumber of n th second harmonic Lamb wave, while k is the wavenumber of the primary Lamb wave. It is noticed that the magnitude of the n th second harmonic Lamb wave $A_n(y)$ is linearly proportional to the propagation distance (y) under the condition of $k_n^* = 2k$ (also called phase velocity matching condition). It is widely accepted that the SHG of the Lamb wave can be significantly affected by the phase velocity matching condition.^{26–30}

B. Influence of the micro-defect on SHG of Lamb wave propagation

As shown in Eq. (4), the value of Δ_n significantly affects the magnitude of the generated second harmonic. For the case of approximate phase velocity matching (i.e., $\Delta_n \approx 0$), the phase velocity of the generated second harmonic is not exactly equal to that of the primary Lamb wave. In this study, the Lamb wave mode pair that approximately satisfies phase velocity matching is

intentionally selected. Consequently, the cumulative effect of the generated second harmonic varies sinusoidally with respect to the propagation distance.^{29,30} Figure 2(a) shows a schematic analysis of the SHG of Lamb wave propagation in a certain distance, under the approximate phase velocity matching condition. For the ease of analysis, the path of Lamb wave propagation is discretized as a series of grids with a designated length. When the primary Lamb wave passes through an arbitrary grid (e.g., the i th grid), the corresponding second harmonic (denoted by $A_{(i)}^{(2\omega)}$) will be generated due to the material nonlinearity.^{29–31} The same phenomenon will take place in its adjacent grid, i.e., the second harmonic (denoted by $A_{(i+1)}^{(2\omega)}$) will be generated when the primary Lamb wave passes through the $(i+1)$ th grid. Due to approximate phase velocity matching, there is a phase difference between $A_{(i)}^{(2\omega)}$ and $A_{(i+1)}^{(2\omega)}$ (denoted by angle $\Delta\varphi$ whose value is proportional to Δn).^{31,32} For the case without micro-defect, the total second harmonic generated by the primary Lamb wave propagating through the path of the transmitter–receiver pair can be determined as $A_a^{(2\omega)} = \sum_{m=1, \dots, i, \dots, j, \dots, N} A_{(m)}^{(2\omega)}$, as shown in Fig. 2(a).³² It should be pointed out that for the case of exact phase velocity matching, there is $\Delta\varphi = 0$ and the total second harmonic generated (i.e., $A_a^{(2\omega)}$) will grow linearly with propagation distance.^{31,32}

When the primary Lamb wave propagates through the path with micro-defect, except for the j th grid including the micro-defect [see Fig. 2(b)], the second harmonic generated in other grids should be the same as that in Fig. 2(a), once the scattering of the primary wave induced by the micro-defect is negligible. It should be pointed out that compared with Fig. 2(a), the phase difference

between the second harmonics generated in $(j-1)$ th and j th grids will change from $\Delta\varphi$ to $\Delta\varphi_s$ due to the geometric variation of the j th grid. Specifically, change in the thickness of the j th grid will induce change in the phase velocities of Lamb waves at fundamental and double frequencies, which will lead to the phase difference between $A_{(j-1)}^{(2\omega)}$ and $A_{(j)}^{(2\omega)}$ different from that between $A_{(i)}^{(2\omega)}$ and $A_{(i+1)}^{(2\omega)}$ [see Fig. 2(b)].^{31,32} For the case with micro-defect, the total second harmonic generated by the primary Lamb wave propagating through the path of the transmitter–receiver pair is formally determined by $A_b^{(2\omega)} = \sum_{m=1, \dots, i, \dots, j, \dots, N} A_{(m)}^{(2\omega)}$, as shown in Fig. 2(b).³² Based on the above analysis, it is expected that the total second harmonic generated by the primary Lamb wave propagating through the path with and without micro-defect is certainly different from each other. Thus, the change in the second harmonic generated in the path of Lamb wave propagation can be used to calculate the SDC for the reconstruction of the micro-defect image.

Specifically, the Lamb wave mode pair of S0 at a frequency of 0.6 MHz and its second harmonic at a frequency of 1.2 MHz are selected in this study. Phase velocity of S0 at 0.6 MHz is a little bit higher than that of the second harmonic generated. When the primary Lamb wave propagates through the region with the local micro-defect, the decrease in the thickness of the j th grid with micro-defect (i.e., smaller frequency-thickness product) will induce the change of phase velocities of Lamb waves at fundamental and double frequencies, as shown in Fig. 3(a). The micro-defect-induced thickness decrease will lead to better phase velocity matching between the primary S0 mode and its second harmonic generated [i.e., $\Delta\varphi > \Delta\varphi_s$ in Fig. 2(b)].^{29–32}

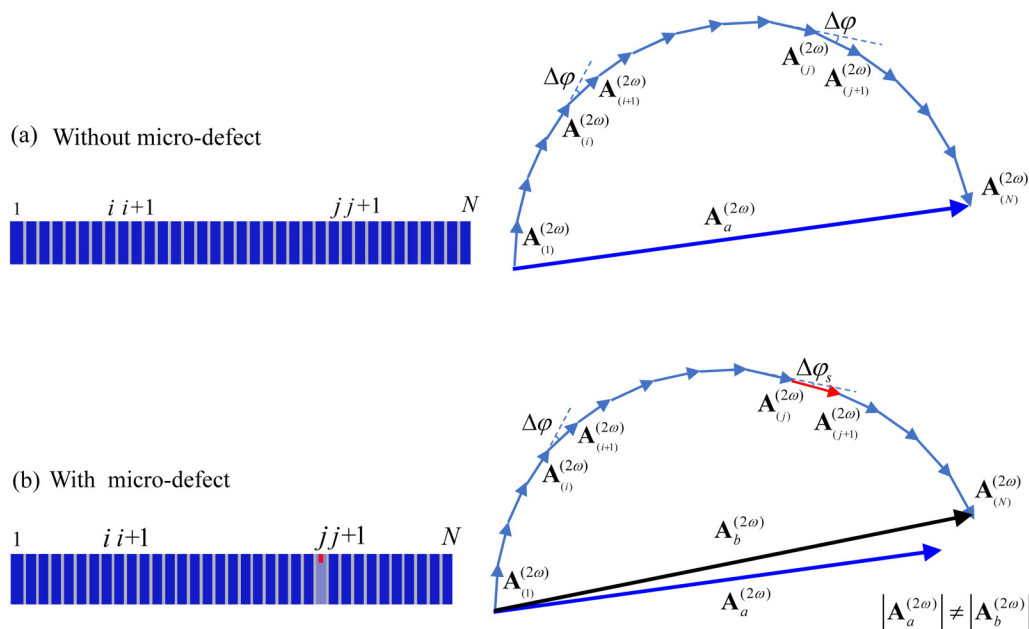


FIG. 2. Schematic analysis of SHG under the approximate phase velocity matching, (a) without micro-defect and (b) with micro-defect.

It needs to be noted that the existence of micro-defect in this investigation causes a better phase velocity matching, which will lead to an increase in the second-harmonic amplitude compared with the case without micro-defect (see Fig. 2). However, under the condition of exact phase velocity matching, the existence of micro-defect will make the above condition no longer be satisfied in the j th grid, which will lead to a decrease in the second-harmonic amplitude.^{32–36} Due to the fact that the imaging method proposed in this study is based on the variation of second-harmonic amplitudes to construct the defect image, it should be applicable regardless of the exact or approximate phase velocity matching.

C. Defect imaging algorithm

The RAPID algorithm is a probabilistic method based on the signal difference to construct damage images.¹⁵ The SDC can be used as a damage index, which represents the statistical difference of the signals in specimen with defect from the one without damage. These image indexes for every possible transducer pairs are spatially distributed and the linear summation generates the damage area image.¹⁵ It can be expressed as

$$\text{SDC}_{tr} = 1 - \left| \frac{\sum_{m=1}^M (X_m - \mu_X)(Y_m - \mu_Y)}{\sqrt{\sum_{m=1}^M (X_m - \mu_X)^2} \sqrt{\sum_{m=1}^M (Y_m - \mu_Y)^2}} \right|, \quad (6)$$

where X is the measured signal and Y is the reference signal. μ_X and μ_Y are the mean values of corresponding signals. M is the length of the data. If the signals have no difference, the SDC value is equal to zero. If the signals are out of phase, the SDC achieves the maximum value of 1.0. The subscripts t and r of SDC represent the transmitter and receiver, respectively.

After calculating all the SDC values, the next step is image reconstruction. We define the distance ratio $R_{tr}(x, y)$ as

$$R_{tr}(x, y) = \frac{\sqrt{(x_t - x)^2 + (y_t - y)^2} + \sqrt{(x_r - x)^2 + (y_r - y)^2}}{\sqrt{(x_t - x_r)^2 + (y_t - y_r)^2}}, \quad (7)$$

where the numerator of the right-hand side of Eq. (7) is the sum of the distances from point (x, y) to transmitter t and from that to receiver r , while its denominator is the distance from t to r .

The image is reconstructed by spatial distribution of SDC values in an elliptical pattern. The shape factor β controls the size of ellipse and is greater than 1.0. The variable shape factor is used to obtain a better image result, which is

$$\beta = R_{\max} \geq 1.0. \quad (8)$$

The spatial distribution function $S_{tr}(x, y)$ decides the SDC value distribution, which is defined as

$$S_{tr}(x, y) = \frac{\beta_q - R_{tr}(x, y)}{\beta_q - 1}, \quad \text{for } \beta_q > R_{tr}(x, y), \quad (9)$$

$$S_{tr}(x, y) = 0, \quad \text{otherwise,}$$

where q is the ordinal number of the used transmitter–receiver pair.

The last step is the calculation of the image amplitude at each pixel, which is the sum of the location probabilistic value from each transmitter–receiver pair. Specifically, it is stated as

$$P(x, y) = \sum_{t=1}^{N-1} \sum_{r=t+1}^N \text{SDC}_{tr} \times S_{tr}(x, y), \quad (10)$$

where N is the total number of the used transmitter–receiver pairs.

III. VALIDATION WITH FINITE ELEMENT SIMULATION

The dispersion curves of Lamb waves propagating in a 1.0 mm thick aluminum plate have been numerically calculated and plotted in Fig. 3. In this investigation, the mode pair consisting of the S_0 mode at the frequency of 0.6 MHz and its second harmonic at the frequency of 1.2 MHz is selected, which approximately satisfies the phase velocity matching condition (the phase velocity of S_0 at 0.6 MHz is a little bit higher than that of its second harmonic).

To verify the schematic analysis of the micro-defect-induced change of the generated second harmonic given in Sec. II, a 2D model with loads and boundary conditions is built by COMOL software,^{37–39} as illustrated in Fig. 4. Third-order elastic constants are selected in the software's library for nonlinear material definition. A micro-defect with the same size as the real one is created in the model. The model is meshed with four-node reduced-integration plane strain elements (CPE4R) through a structured meshing algorithm. The maximum element size and time step are adopted based on the following equation to obtain adequate accuracy and high efficiency of simulation,

$$\Delta l = \lambda_{\min}/20, \quad (11)$$

$$\Delta t = 1/20f_{\max}, \quad (12)$$

where Δl is the element size and Δt is the time step, and λ_{\min} and f_{\max} are the shortest wavelength and highest frequency of interest, respectively. The element size of this study is chosen as 0.1 mm, and the time step as 1×10^{-7} s.

A Hanning-windowed sinusoidal tone burst consisting of 15 cycles with a central frequency of 0.6 MHz is used as the excitation signal. More details about the constructions of the numerical model can also be found in our earlier publication.³⁸ As shown in Fig. 5(a), a slight phase shift caused by the micro-defect in the traveling path can be observed in the measured time-domain signals. Meanwhile, a clear variation in the second-harmonic amplitude can be found in Fig. 5(b), which is consistent with the theoretical prediction given in Sec. II B.

IV. EXPERIMENTAL CONSIDERATIONS

A. Specimens and used sensors array

The specimens under investigation are rectangular 1060 aluminum plates with geometrical dimensions of $350 \times 350 \times 1.0$ mm³. The artificial micro-defect at different locations has been introduced in the plate with a length of 20 mm and the width of about

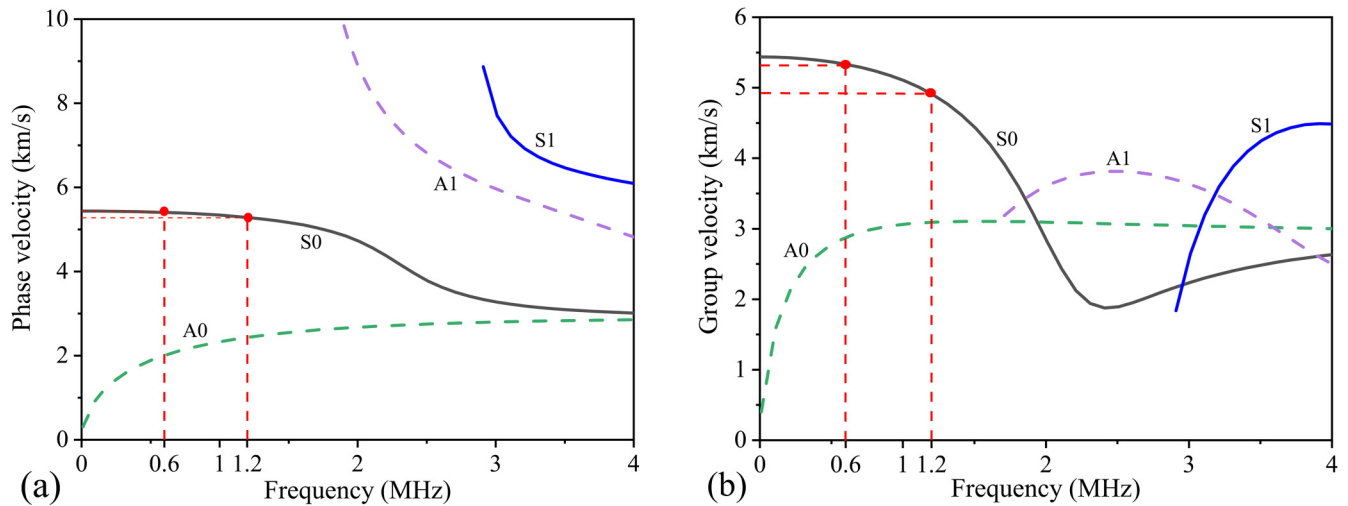


FIG. 3. Dispersion curves of Lamb wave propagation in the 1060 aluminum plate: (a) phase velocity and (b) group velocity.

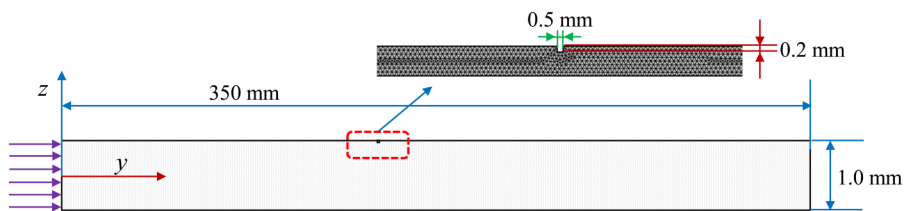


FIG. 4. Schematic of a 2D model used for FE simulation.

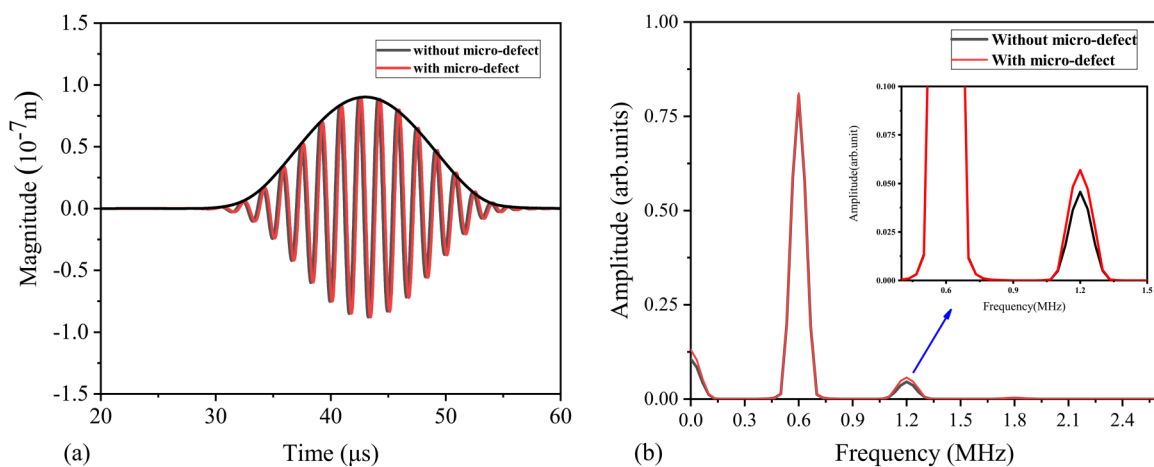


FIG. 5. Numerical simulation of micro-defect-induced variation of the time-domain signals (a) and the corresponding amplitude-frequency curves (b).

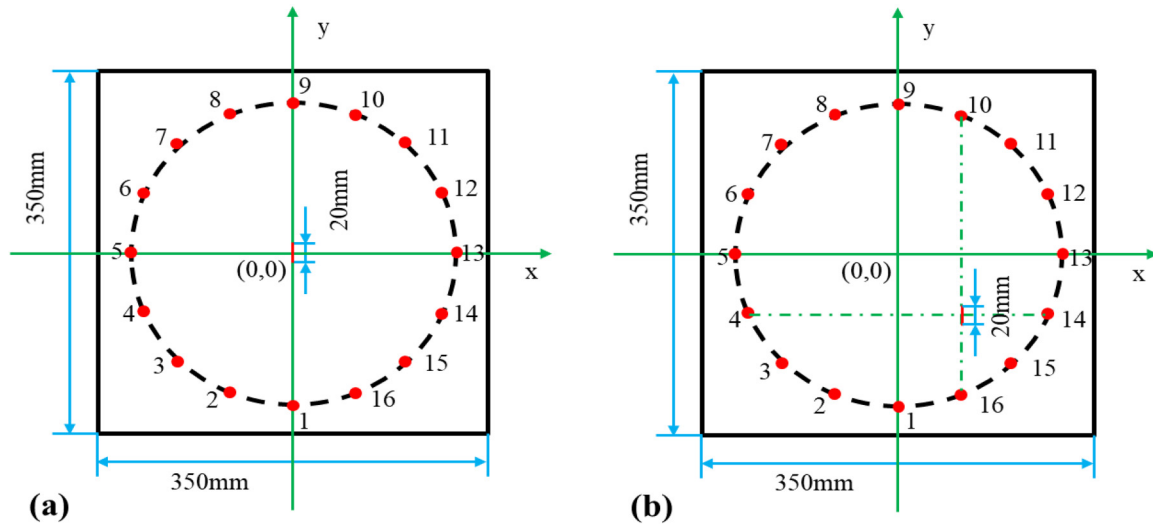


FIG. 6. The surface defect in specimen No. 1 (a) and specimen No. 2 (b).

0.5 mm (smaller in one order of magnitude than the wavelength). It is important to note that the defect with 0.5 mm width and 0.2 mm depth is created in the numerical model, while the length of the defect is not concerned since the numerical simulation is carried out in a 2D model built by COMSOL software. It is the effective numerical simulation built by the 2D model to verify the analysis of Lamb wave propagation.^{37–39} In the experiment, a 3D defect, which has the same width and depth as the numerical one but has a certain length within the sensor array region, is introduced in the sample, as shown in Fig. 6.

In this study, the sensors' array is configured as round shape for the reason that this setup can ensure the consistent distance of all propagation paths from different transmitter–receiver pairs. For

different propagation paths, the variation in generated second harmonic is only attributed to the existence of micro-defect in the path. Thus, round shape of the sensors' array is chosen in this investigation. The sensor positions in the specimens with all possible transmitter–receiver paths are shown in Fig. 7, where the sensor array consists of eight transmitter–receiver pairs (16 sensors in total) that have been mounted in a round shape.

B. Experimental setup

The schematic diagram of the experiment setup for one transmitter–receiver pair is shown in Fig. 8. The RAM 5000 SNAP ultrasonic system is connected to a computer for parameter setting and signal analysis. A sinusoidal tone-burst of 15 cycles at the frequency of 0.6 MHz is generated by this system. The generated signal then passes through an attenuator to purify the incident signal for a high signal-to-noise ratio. The expected Lamb wave mode is excited by means of oblique incidence, and the corresponding incident angle is determined by Snell's law. The transducers are clamped to the acrylic wedges. Light lubrication oil is used to couple the transducers to the wedges as well as the wedges to the sample.

For each transmitter–receiver pair, a sinusoidal tone-burst signal generated by the ultrasonic system is first applied to the transmitter, and then the corresponding time-domain signal is detected by the receiver. Next, let all the conditions be kept unchanged except for phase-reversal for the carrier of the sinusoidal tone-burst voltage applied to the same transmitter and then repeat the same measurement. Thus, for each transmitter–receiver pair, two tests with the same setup but a reversal phase of the excitation signal are carried out experimentally. The same measurements are conducted in other transmitter–receiver pairs.

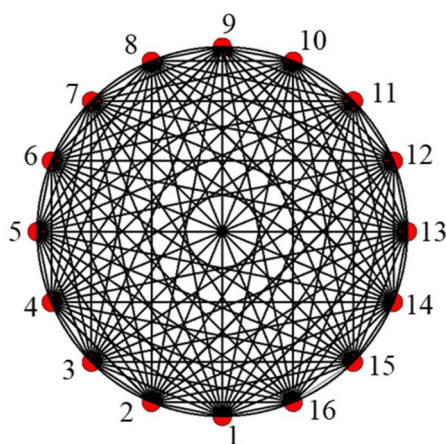


FIG. 7. Sensors' array configuration and all wave beam paths.

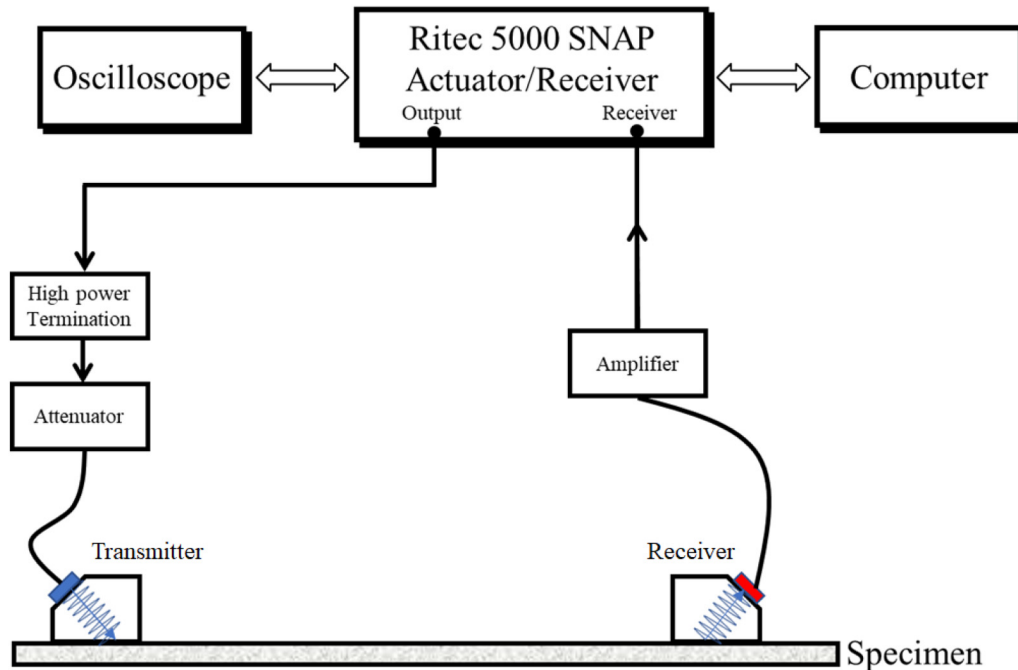


FIG. 8. Scheme of the experimental setup for one transmitter-receiver pair.

V. EXPERIMENTAL RESULTS

A. Image reconstruction using linear time-domain signals

The conventional linear Lamb wave tomographic approach has been first applied to reconstruct the image of the micro-defect. Linear Lamb wave tomography is based on the calculation of amplitude differences of the signal in the time domain. As shown in Fig. 9, two typical signals received from the specimen with and without micro-defect are basically overlapped. It is hard to identify any difference between the two linear time-domain signals of Lamb waves that propagate through the region with and without micro-defect. The value of SDC calculated by the tiny variation in the time-domain amplitude almost equals zero. The micro-defect image reconstructed by the linear time-domain signals is shown in Fig. 10. It is found that there is no visualized information obtained about the shape and size of the micro-defect. Therefore, it can be concluded that the linear Lamb wave tomographic approach is not effective to identify and image the micro-defect of this size.

B. Image reconstruction using the SHG of Lamb wave propagation

Considering the fact that the SHG of Lamb wave propagation can be influenced by the existence of micro-defect in the propagation path, as illustrated in Secs. II and III, variation in the generated second-harmonic amplitudes can be used for the calculation of SDC to construct the micro-defect image. Amplitudes of the

generated second harmonics in the frequency domain are employed to reconstruct the micro-defect image. It can be found that the frequency-domain signals obtained by fast Fourier transform mainly contain the primary wave and the second harmonic generated. Figure 11 shows the measured signals in the time domain at

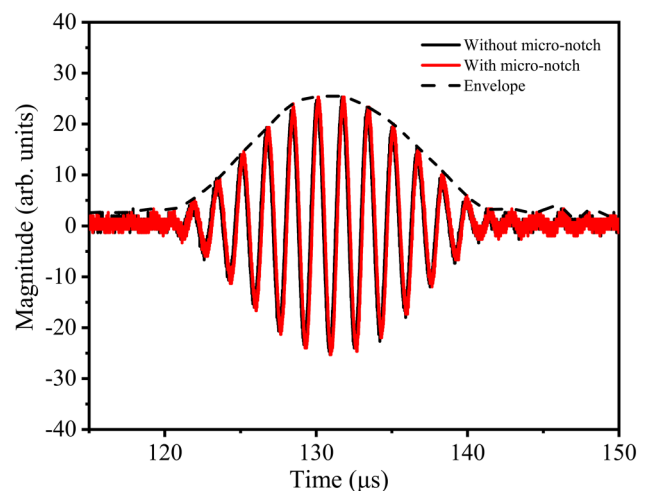


FIG. 9. Comparison of signals in the paths with and without micro-defect in the time domain.

reverse phase and the superimposed signals acquired from the path without micro-defect. Obviously, the superimposed signals counteract the two signals out of phase, as shown in Fig. 11.

The frequency spectrum of the measured Lamb wave signals is shown in Fig. 12. The black dashed line represents the amplitude–frequency curve of the signals without phase-reversal processing. It can be found that the amplitude of the generated second harmonic (at double frequency of fundamental one) is very tiny compared with that of the primary wave. Generally, the amplitude of the generated second harmonic is too tiny to be effectively extracted. Therefore, the phase-reversal technique is employed here to counteract primary waves and accentuate generated second harmonics synchronically. Due to the dispersive nature of Lamb waves, the approximate or exact phase velocity matching (i.e., synchronism condition) for the selection of the Lamb wave mode pair is essentially needed to employ the phase-reversal technique to counteract the primary waves and accentuate the second harmonics generated.^{30–36} The red solid line shown in Fig. 12 represents the amplitude–frequency curve of the measured signals after phase-reversal processing. It is found that primary waves at the fundamental frequency are almost eliminated. In contrast, only the second harmonic plays a dominant role in the frequency domain. The second-harmonic amplitude of the measured signal is twice of that before phase-reversal processing, as shown in Fig. 12.

Referring to the above process, comparison of the amplitude–frequency curves obtained by processing the measured signals in the paths with and without micro-defect is provided in Fig. 13. The black solid line represents the frequency–amplitude curve of the measured signal in the path without micro-defect, while the red one represents that in the path with micro-defect. As shown in Fig. 13, the variation in the generated second-harmonic amplitude has been clearly observed. It is also noted that the amplitude of the primary wave at the fundamental frequency is not completely

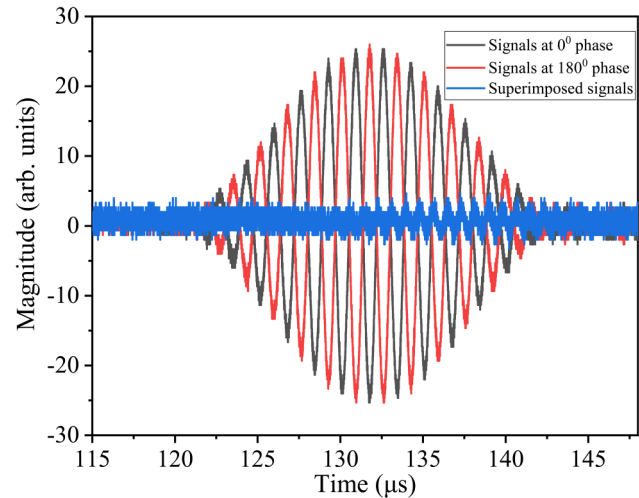


FIG. 11. The time-domain signals at the phase of 0° and 180° and the superimposed signals propagating in the path without micro-defect.

eliminated. This phenomenon may be attributed to the instability of coupling conditions or the influence of ambient noise in repeated measurements. The increase in the second harmonic of the Lamb wave propagating through the path with micro-defect has been well explained and verified numerically. The obtained experimental result is in good agreement with the numerical one shown in Fig. 5, which clearly illustrates the effect of the micro-defect on the SHG of Lamb waves. Hence, the second-harmonic amplitudes obtained by phase-reversal processing with and without defect can be used to effectively calculate the SDC values.

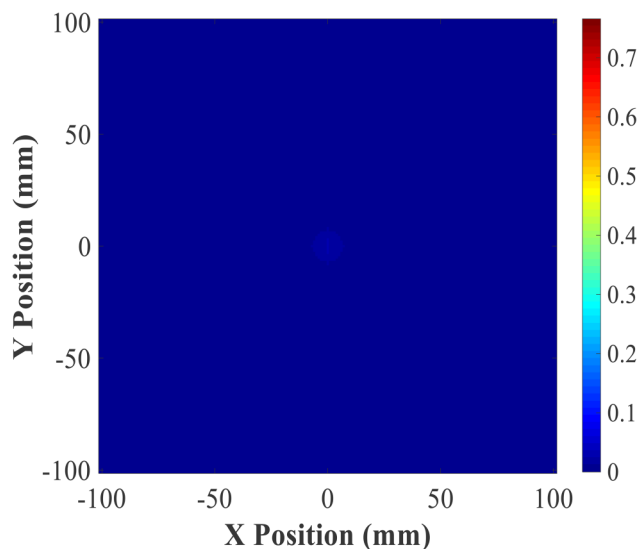


FIG. 10. Image construction of the defect using the linear time-domain signals.

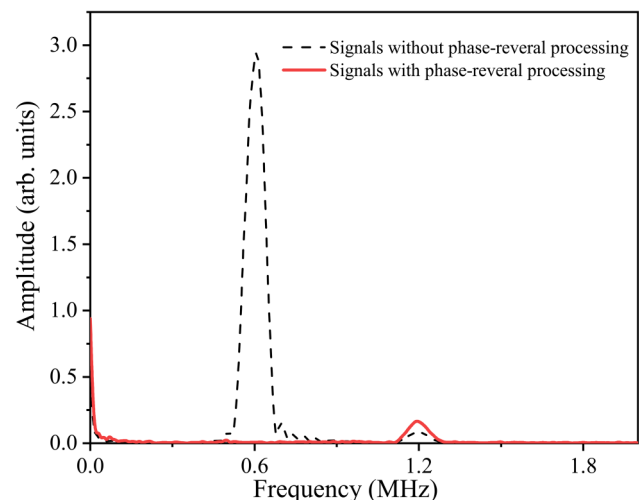


FIG. 12. Comparison of amplitude–frequency curves without and with phase-reversal processing.

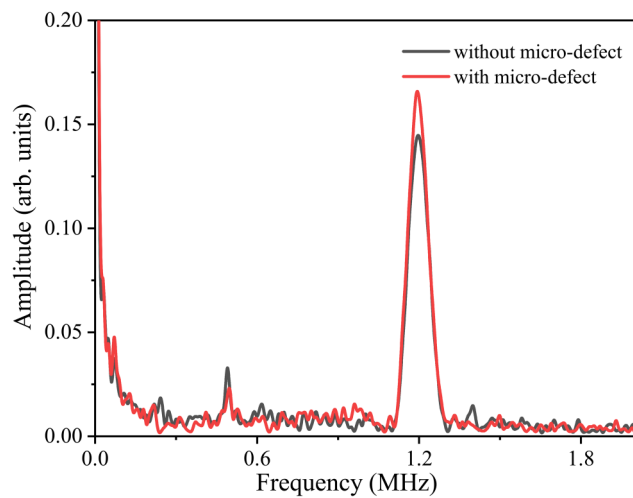


FIG. 13. Comparison of amplitude–frequency curves by phase-reversal processing with and without micro-defect.

To construct the image of the micro-defect, the SDC value is calculated by the differences in the second-harmonic amplitudes of Lamb waves. Combining the SDC of each transmitter–receiver path, the image reconstruction result of the micro-defect in specimen No. 1 before and after the phase-reversal approach are obtained and shown in Fig. 14. It clearly illustrates that the combination of the phase-reversal approach and the RAPID algorithm can be used to effectively image the micro-defect. The resolution of the constructed image is obviously improved by the proposed approach.

The RAPID algorithm actually uses the SDC to generate a statistical comparison of different paths in the specimen. As shown in Fig. 14, the

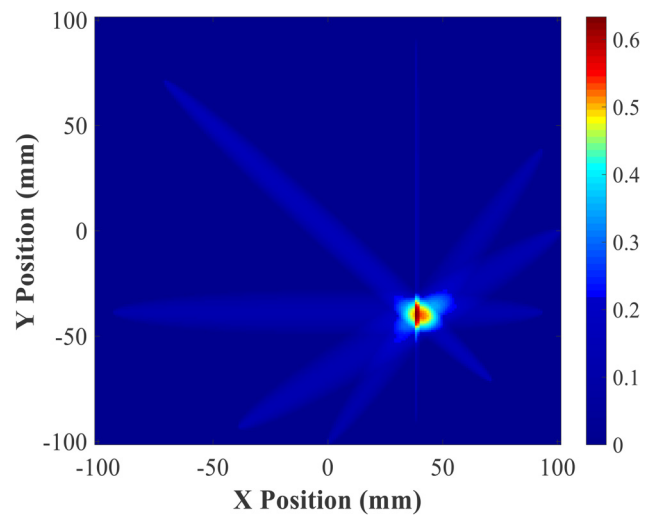


FIG. 15. Image reconstruction of specimen No. 2 using a phase-reversal approach.

obtained results indicate that different propagation paths of the transmitters–receiver pairs have different effects for imaging. When the propagation path is parallel to the defect length (i.e., defect lies directly on a line of sight), there is less effect for imaging the defect than the case where the wave path is non-parallel to the defect length. The results show that the proposed method has a potential to identify the defect orientation.

In addition, it is known that the reconstructed images can be significantly affected by the number and placement of the array transducers.^{15–18} Considering the fact that the propagation distance can affect the cumulative effect of generated second harmonic of

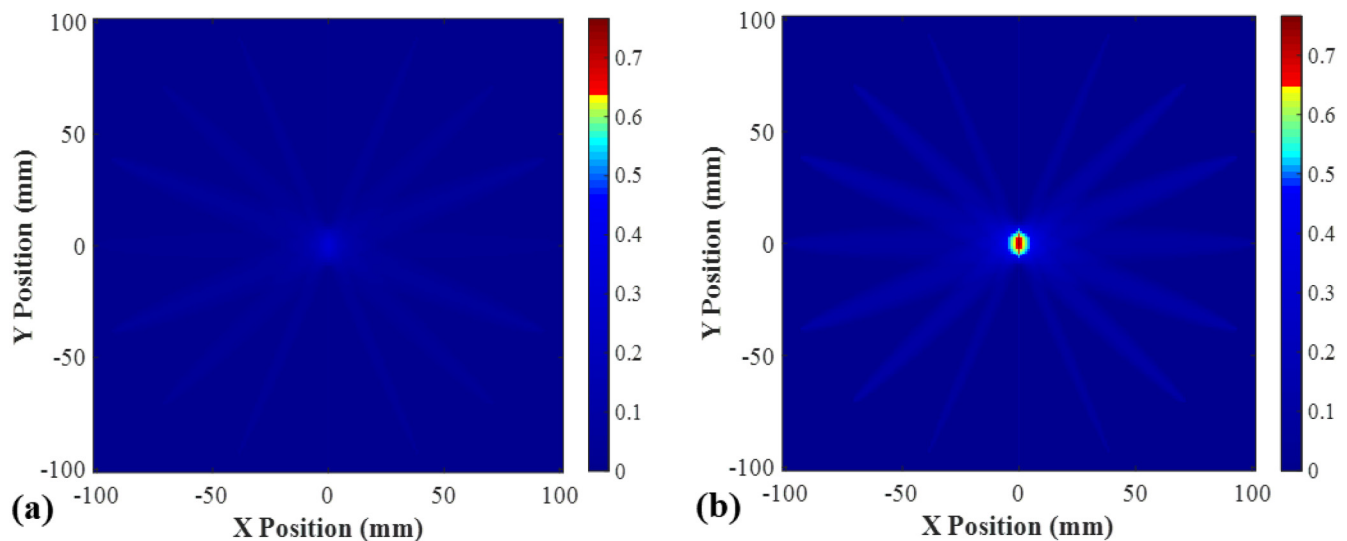


FIG. 14. Image reconstruction by SHG of specimen No. 1 before (a) and after (b) phase-reversal approach.

the primary Lamb wave, the sensors' array is configured as round shape in this study since this setup can ensure the consistent propagation distance for all transmitter–receiver pairs. If the array shape is fixed, more number of transducers used in the array will achieve a better resolution of imaging results.

The proposed technique is also used to identify and image the micro-defect in different locations. The reconstructed image of the micro-defect in specimen No. 2 is shown in Fig. 15. The image of the micro-defect with location information is reconstructed with a satisfactory resolution. It indicates that the effectiveness of the proposed technique is verified for identification and imaging of the micro-defect of this size range, with an improved resolution.

VI. CONCLUSIONS

In this study, the SHG of Lamb waves is applied to detect the small geometric defect that is not associated with the non-classical acoustic nonlinearity. The combination of the SHG of Lamb waves and the Lamb wave tomographic approach is employed to effectively obtain the micro-defect image. The mechanism and the effect of micro-defect-induced variation in the generated second harmonic of Lamb wave propagation are analyzed and verified numerically and experimentally. Variations in second-harmonic amplitudes caused by the micro-defect have been successfully observed and used to calculate the SDCs for image reconstruction. Moreover, the phase-reversal technique is employed to enhance the signal-noise ratio of the generated second harmonic of Lamb wave propagation. The image of the micro-defect has been successfully reconstructed with an improved resolution by the proposed method.

ACKNOWLEDGMENTS

This work was supported by the National Natural Science Foundation of China (NSFC) (Grant Nos. 12134002, 11974295, 12074050, and 11834008). It was also supported by the project of Basic Technology Research, which is funded by Technology and Quality Division of the Ministry of Industry and Information Technology of China (Grant No. JSZL2018602C001) and the Principal Fund of Xiamen University (Grant No. 20720210040).

AUTHOR DECLARATIONS

Conflict of Interest

The authors have no conflicts to disclose.

DATA AVAILABILITY

The data that support the findings of this study are available within the article.

REFERENCES

- 1J. L. Rose, *J. Pressure Vessel Technol.* **124**, 273 (2002).
- 2D. N. Alleyne and P. Cawley, *IEEE Trans. Ultrason. Ferroelect. Freq. Control.* **39**, 381 (1992).
- 3W. Li, Y. Cho, and J. D. Achenbach, *Smart Mater. Struct.* **21**, 085019 (2012).
- 4T. Kundu, *Nonlinear Ultrasonic and Vibro-Acoustical Techniques for Nondestructive Evaluation* (Springer International Publishing, 2019).
- 5S. V. Walker, J. Y. Kim, J. Qu, and L. J. Jacobs, *NDT&E Int.* **48**, 10 (2012).
- 6C. Zhou, M. Hong, Z. Su, Q. Wang, and L. Cheng, *Smart Mater. Struct.* **22**, 015018 (2013).
- 7N. Rauter and R. Lammering, *Mech. Adv. Mater. Struct.* **22**, 44 (2015).
- 8Y. Xiang, M. Deng, and F. Xuan, *J. Appl. Phys.* **115**, 044914 (2014).
- 9V. K. Chhillara and C. J. Lissenden, *Opt. Eng.* **55**, 011002 (2016).
- 10C. J. Lissenden, Y. Liu, and J. L. Rose, *Insight* **57**, 206 (2015).
- 11H. Sohn, H. J. Lim, M. P. DeSimio, K. Brown, and M. Derriso, *J. Sound Vib.* **333**, 1473 (2014).
- 12K.-Y. Jhang, *Int. J. Precis. Eng. Manuf.* **10**, 123 (2009).
- 13K. E.-A. Van Den Abeele, P. Johnson, and A. Sutin, *Res. Nondestruct. Eval.* **12**, 17 (2000).
- 14I. Y. Solodov, *Ultrasonics* **36**, 383–390 (1998).
- 15T. Hay, R. Royer, H. Gao, X. Zhao, and J. Rose, *Smart Mater. Struct.* **15**, 946 (2006).
- 16X. Zhao, R. L. Royer, S. E. Owens, and J. L. Rose, *Smart Mater. Struct.* **20**, 105002 (2011).
- 17X. Zhao, H. Gao, G. Zhang, B. Ayhan, F. Yan, C. Kwan, and J. L. Rose, *Smart Mater. Struct.* **16**, 1208 (2007).
- 18J. K. V. Velsor, H. Gao, and J. L. Rose, *Insight* **49**, 532 (2007).
- 19B. Sheen and Y. Cho, *Int. J. Precis. Eng. Manuf.* **13**, 671 (2012).
- 20W. Li and Y. Cho, *Ultrasonics* **65**, 87 (2016).
- 21A. Viswanath, B. P. C. Rao, S. Mahadevan, T. Jayakumar, and B. Raj, *J. Mater. Sci.* **45**, 6719 (2010).
- 22M. Fukuda and K. Imano, *Jpn. J. Appl. Phys.* **51**, 07GB06 (2012).
- 23Y. Xiang, M. Deng, C. Liu, and F. Xuan, *J. Appl. Phys.* **117**, 214903 (2015).
- 24S. Shan, L. Cheng, and P. Li, *Smart Mater. Struct.* **26**, 025019 (2017).
- 25Q. Ma, Y. Ma, X. Gong, and D. Zhang, *Ultrasound Med. Biol.* **31**, 889 (2005).
- 26W. Li, S. Hu, and M. Deng, *Materials* **11**, 1961 (2018).
- 27M. Deng, Y. Xiang, and L. Liu, *J. Appl. Phys.* **109**, 113525 (2011).
- 28W. Li, B. Chen, and Y. Cho, *Appl. Acoust.* **160**, 107124 (2020).
- 29M. Deng, *J. Appl. Phys.* **94**, 4152 (2003).
- 30W. J. N. de Lima and M. F. Hamilton, *J. Sound Vib.* **265**, 819 (2003).
- 31M. Deng, *Nonlinear Lamb Waves in Solid Plate* (Science Press, Beijing, 2006), pp. 74–76.
- 32M. Deng, P. Wang, and X. Lv, *J. Phys. D: Appl. Phys.* **38**, 344 (2005).
- 33M. Sun, Y. Xiang, M. Deng, B. Tang, W. Zhu, and F. Xuan, *Appl. Phys. Lett.* **114**, 011902 (2019).
- 34T. M. Ye, S. Biwa, and N. Mori, *J. Acoust. Soc. Am.* **148**, 2073 (2020).
- 35S. Shan and L. Cheng, *Ultrasonics* **119**, 106554 (2022).
- 36A. Aseem and C. T. Ng, *NDT&E Int.* **122**, 102496 (2021).
- 37M. Li, M. Deng, G. Gao, and Y. Xiang, *J. Sound Vib.* **421**, 234 (2018).
- 38W. Li, Y. Xu, N. Hu, and M. Deng, *AIP Adv.* **10**, 045119 (2020).
- 39X. Wan, P. Tse, X. Zhang, G. Xu, Q. Zhang, H. Fan, Q. Mao, M. Dong, C. Wang, and H. Mao, *Smart Mater. Struct.* **27**, 045006 (2018).